

Damage Localisation in Fresh Cement Mortar Observed via In Situ (Timelapse) X-ray μ CT imaging.

Authors Names and Affiliations

Petr Miarka^{a,b,*}, Daniel Kytýř^c, Petr Koudelka^c, Vlastimil Bílek^d

^aCzech Academy of Sciences, Institute of Physics of Materials, Žitkova 22, 616 00 Brno, Czech Republic

^bBrno University of Technology, Faculty of Civil Engineering, Veverří 331/95, 602 00 Brno, Czech Republic

^cCzech Academy of Sciences, Institute of Theoretical and Applied Mechanics, Prosecká 76, Prague 9, Czech Republic

^dVŠB — Technical University of Ostrava, Faculty of Civil Engineering, Ludvíka Podéště 1875/17, 708 00 Ostrava-Poruba, Czech Republic

*Corresponding Author:

Petr Miarka (email: miarka@ipm.cz). Tel: +420 532 290 430

Abstract

This paper studies the evolution of internal damage in fresh cement mortar over the 25 hours of hardening. In situ timelapse X-ray computed micro-tomography (μ XCT) imaging method was used to detect internal damage and capture its evolution in cement hydration. During μ XCT scans, the hydration heat was measured, which provided insight for the internal damage evolution with a link to hydration heat development. The measured hydration heat was compared with an analytical prediction, which showed a relatively good agreement with the experimental data. Using 20 CT scans acquired throughout the observed cement hydration, it was possible to obtain a quantified characterisation of the porous space. Additionally, the use of timelapse μ XCT imaging over 25 hours allowed to study the crack growth inside of the meso-structure including its volume and surface. Observed results provide valuable insights to cement mortar shrinkage.

Keywords: Hydration; Portland cement; X-ray μ CT; Crack; Porosity;

Highlights

- In situ timelapse X-ray μ CT scanning of cement hydration.
- X-ray μ CT analysis of crack growth in cement mortar.
- Measured and analytically calculated hydration heat.
- Porosity quantified using μ XCT data.
- Crack propagation, volume and surface in 3D from μ XCT.

Abbreviations

2D/3D	two-/three-dimensional	CM	cementitious materials
AE	acoustic emission	MS	meso-structure
DIC	digital image correlation	OPC	ordinary Portland cement
μ XCT	X-ray computed micro-tomography	ROI	region of interest
SCM	supplementary cementitious materials		

Nomenclature

D	specimen's diameter [mm]	H_T	ultimate hydration heat [J/g]
C_g	centre of gravity	C_C	CM content [g/m ³]
L	specimen's length [mm]	t_e	equivalent time [hours]
T	temperature [°C]	t	time [hours]
T_c	concrete temperature [°C]	c_p	specific heat capacity [J·kg ⁻¹ ·K ⁻¹]
T_r	room temperature [°C]	E	activation energy [J/mol]
ΔT	temperature difference [°C]	R	universal gas constant [8.314 J/mol·K ⁻¹]
Q_H	rate of heat hydration [J/m ³]	$\alpha(t_e)$	degree of hydration at t_e [-]
$Q_{X\text{-ray}}$	heat generated by X-ray source [J/m ³]	α_u	ultimate degree of hydration [-]
Q_{tot}	total heat [J/m ³]	β	hydration shape parameters [-]
h_1	height [mm]	ρ	concrete density [kg·m ³]
H	hydration heat [J/g]	τ	hydration time parameter [hours]
H_u	total hydration heat of CM [J/g]		

1. Introduction

Regardless of noticeable improvements in strength and overall performance of modern concrete materials i.e., high performance concrete (HPC) [1] and high strength concrete (HSC) [2], are sensitive to form micro-cracks, which can increase in size over the structure's lifespan. Such modern materials are being developed to meet high environmental demands i.e., CO₂ emissions [3–5] and to consume fewer natural resources [6,7] (water, aggregates, additives) in concrete production, with motivation to enhance their mechanical performance and improving their durability, while reducing their overall cost.

Nonetheless, the ordinary Portland cement (OPC) is still being used in pure form or as a blended systems [8] in most of the mixtures as it has reliable properties. OPC hydration is an exothermic process [9], and the total heat generated can have significant influence on the in-place performance of concrete structures. Early hydration of OPC [10] and its modelling is studied by various models [11].

HPC is sensitive to form micro-cracks, which can increase in size over the structure's lifespan. These micro-cracks with combination of aggressive/hostile environment can lead to serious durability issues as they can be present mainly in the protective cover layer [12]. Origin of these micro-cracks is in various load actions i.e., temperature, static or cyclic loading and rheology of concrete itself [13], especially, autogenous shrinkage [14,15]. Generally, the mechanisms of concrete fracture are complex due to highly heterogenous inner structure consisting of aggregates, cement paste and air pores [16]. This complex behaviour is often studied by various fracture test setups.

In laboratory conditions, concrete fracture process can be studied by numerous experimental methods often under a quasi-static loading e.g., Moiré interferometry [17,18], acoustic emission (AE) [19], digital image correlation (DIC) [20–22], neutron tomography [23,24] and X-ray computed tomography [25,26]. Especially, X-ray computed micro-tomography (μ XCT) scanning has attracted a growing interest [27] in material science and experimental mechanics research fields as it allows for non-destructive, high-resolution 3D analysis of material morphology and internal damage localisation. The 3D model of analysed samples is virtually reconstructed from 2D X-ray images/projections obtained at a different angle resulting to a spatial resolution, depending on the sample size, often less than 50 μ m [28].

From the concrete technology viewpoint μ XCT allows for precise measurement of internal flaws i.e., pores [29], cracks [30,31], inclusions [32], and more importantly it allows for comprehensive analysis of material heterogeneity [33]. Thus, employment of μ XCT scans during the loading of quasi-brittle

materials is ideal to study damage evolution at the inner interface - at aggregate/cement paste level. Moreover, μ XCT could be used to study of early age properties and pore structure [34,35], allows for direct observation of C_3S particles [36] and provides insights to internal hydration behaviour [37].

Previous μ XCT studies were focusing on the analysis of damage propagation in quasi-brittle materials under a quasi-static [26,31,38,39] or dynamic [28] loading conditions. Such studies were capturing the μ XCT scans while holding the specimens under constant stress or constant deformation during the scanning process. This scanning method, unfortunately, cannot be extended to fresh cement mortars or mortars due to lack of solid phases, which can carry out the load. Thus, we have decided to measure the hydration temperature to link the obtain μ XCT scans with hydration process.

This experimental study has placed focus on the analysis of the hydration of OPC mortar and its natural process of heat release during cement mortar hardening. For this cylindrical samples with a cement mortar of water to cement ratio w/c of 0.4 were made and the damage evolution in the internal meso-structure (MS) was observed by the μ XCT timelapse scanning setup. The specimens were attached with thermocouples to measure the temperature created by cement hydration. Prior to μ XCT scans, chemical composition, adiabatic hydration temperature and mechanical strengths were measured. The observed experimental results are linked to the damage present in the material's MS. The inner MS and the damage localisation were analysed by μ XCT technique at different time of cement hardening. Found experimental results show the progressive damage in MS, which is governed by the natural exothermic reaction of Portland cement hydration and provides valuable insights to processes governed by cement mortar shrinkage.

2. Materials and Experimental Details

In this section we give a comprehensive overview of studied material and used experimental methods. First, we introduce cement mortar mixture composition and chemical composition of used Portland cement. This is followed by presentation of used geometry. Afterwards, μ XCT test setup together with temperature measurement and method for porosity assessment are presented. These selected methods provide solid base for understanding of this challenging problem of fresh cement mortar hydration.

2.1 Mixture Composition

Portland cement CEM I 42.5 R was used as the binder with a constant dosage of polycarboxylate superplasticizer Glenium 300 (BASF, Germany). The natural sand 0/4 mm represents fine aggregates. Used sand and its sieve curve are presented in Figure 1.

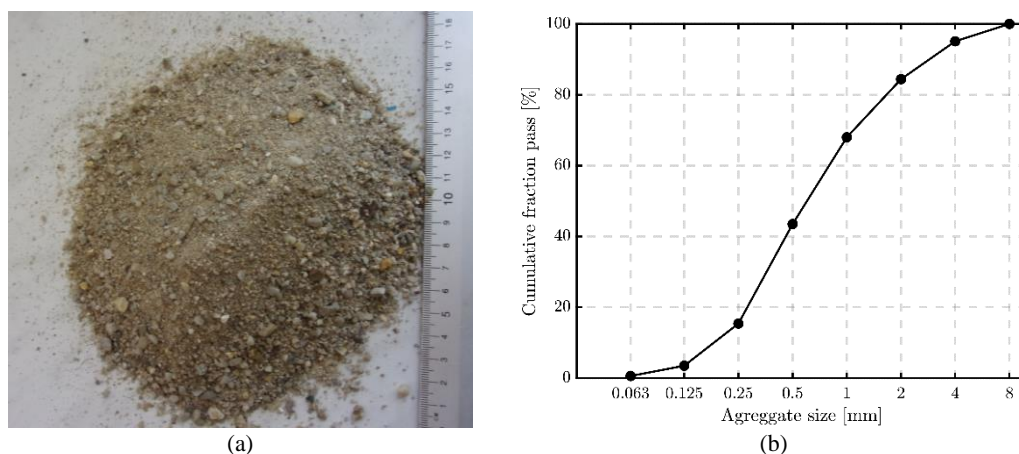


Figure 1: Comparison of used aggregates – (a) fine natural aggregate sand 0/4 and (b) – sieve curve of used sand.

The studied mixture was mixed in small volume batch of 0.8 l and poured directly into the plastic mould. The mixing, setting and testing of studied cement mortar were performed in a room used for X-ray μ CT imaging (outside of laboratory conditions). All the specimens were covered with lid immediately after mixing to prevent excessive water exchange with the environment.

The studied cement mortar is composed to represent HPC with cement to water ratio w/c 0.4. The lack of coarse aggregates in this mixture, is to increase special resolution of the μ XCT imaging and speed up post-processing of the obtained μ XCT data. Thus, only three phase material is analysed. The composition of studied mixture per 0.8 l is shown in Table 1.

Table 1: Material composition of the studied cement mortar per 0.8 l.

Volume	CEM I 42.5R [g]	Water [g]	Sand 0/4 [g]	Superplasticizer (Glenium 300) [g]
0.8 l	712	213	1 423	12

Table 1 shows cement mortar composition per small batch of 0.8l, while the standard mixture composition is per m^3 . This presentation is used to provide the most accurate data to the reader. On the other hand to provide comparison with standard mixture design the cement content per $1 m^3$ is 890 kg.

The mechanical properties were measured in accordance with European standards prior to μ CT scanning procedure and are presented in Table 2.

Table 2: Mechanical parameters (mean values with their standard deviations) of the studied cement mortar mixtures at various age days.

Age [hours/days]	Volume density ρ [kgm^{-3}]	Compressive strength f_c [MPa]	Flexural strength $f_{c,t}$ [MPa]
12 hours	2351 ± 9	3.6 ± 0.1	0.6
24 hours	2341 ± 12	35.3 ± 0.2	5.3
28 days	2376 ± 12	85.4 ± 2.1	10.3

Table 2 shows compressive and flexural strengths at various age in order to capture strength development of the mortar. 12 hours strength was measured as the mortar was hardened enough to allow demoulding and could carry the load. Additionally, the 12 hours age is when the hydration of the cement has its peak. Other strengths i.e., 24 hours and 28 days were measured to provide comparison with standard tests seen in literature.

Besides the mechanical properties, a chemical composition of used Portland cement CEM I 42.5R was measured as the content of mineral has crucial role on the hydration heat development. The measured chemical composition of used CEM I 42.5R is shown in Table 3.

Table 3: Chemical and mineralogical composition in percentage by weight (max. wt. %) of Portland cement CEM I 42.5R.

SiO ₂	Al ₂ O ₃	FeO ₂	CaO	Free CaO	SO ₃	K ₂ O	C ₃ S	C ₂ S	C ₃ A	C ₄ AF
19.9	5.7	2.9	62.6	2.1	6.5	1.0	58	12	9	7

Table 3 shows chemical composition of Portland cement CEM I 42.5R obtained by X-ray fluorescence (XRF) using XL3t – 980 (Thermo Fisher Scientific, USA). The obtained chemical composition served as input to the mineralogical model proposed recently by Shim et al. [40], which combines approach by well-known Bogue's approach [41] with up-to-date findings. The clinker minerals were calculated, and the results were compared with standards.

Since the Portland cement hydration is an exothermic reaction, the heat released during the reaction does not have a steady rate or a steadily changing rate. Thus, the hydration heat development can be separated into three hydration phases based on release rates [42,43]: (1) a short and immediate period of rapid heat decrease, (2) a longer period of steady temperature rise; and (3) temperature decline followed by brief increase in heat emission before stable steady decline to room or outside environment temperature. The first phase is the time when the dry cement first comes into contact with water and corresponds to the initial hydration at the surface of the cement particles, mainly involving C₃A. This follows with the so-called dormant period, at which the rate is very or nearly zero. The second phase typically has its peak at the age of 10 hours, which can change depending on the composition of the mixture. This is related to the connection between individual cement grains.

Correct hydration of OPC influences the future strength development, thus the hydration heat was measured in adiabatic conditions using calorimeter TAM AIR (TA Instruments, USA). Hydration heat was measured for two cement mortars (including cement and sand) with superplasticizer Glenium 300 and without, respectively. The total weight of mortars used was 10.83 g and 10.89 g, respectively. Hydration heat of the mortars was measured over 7 days (168 hours) i.e., when the heat of both samples reached a similar value. The measured hydration temperature is presented in Figure 2. Please note, that the hydration heat is presented in double logarithmic coordinates as the time frame is long and the difference in the temperature would not be visible in standard coordinate system.

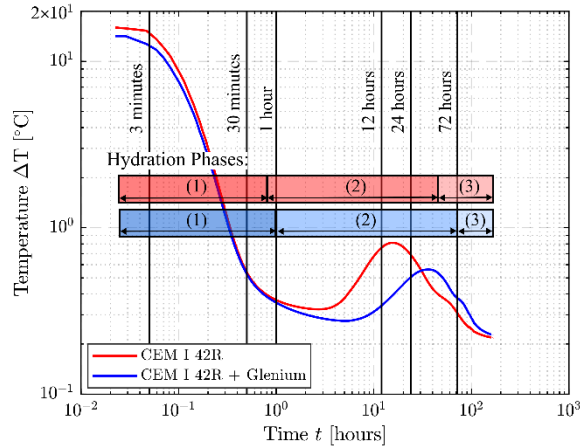


Figure 2: Adiabatic hydration heat development of Portland cement CEM I 42.5R.

Figure 2 shows hydration heat development of two OPC mortar samples with marked hydration phases. Both samples have similar heat development until 0:30 hour to 1 hour with peaks of 16 °C and 18 °C, respectively in first 3 minutes. Afterwards, the hydration heat shows typical rapid decrease. The influence of superplasticizer is clearly visible, as the second peak in hydration heat is delayed to approx. 48 hours, while the plain sample evince its peak at nearly 12:30 hours after mixing.

The difference in hydration heat of both samples starts to be at 0:30 hour in which the sample without the plasticizer starts to produce heat (slowly goes outside the dormant period), whereas the sample with the plasticizer extends its dormant period until 6 hours from mixing. Thus, the difference in dormant period can be is approximately 3 hours.

2.2 Specimen's geometry

In this experimental study, we have selected geometry that allows for reasonable spatial resolution of μ CT images with special attention paid to the container clamped on the rotary table of the CT system, i.e., low X-ray attenuation and geometry to allow acquisition of radiograms with high signal to noise ratio for further volumetric data reconstruction and post-processing. Thus, we have selected cylindrical specimens with diameter D of approx. 29 mm with a length L of 140 mm. Moreover, the container's walls were selected to be X-ray transparent i.e., made of plastic material in this case from polyethylene (PE). The dimension of the used cylinder is shown in Figure 3

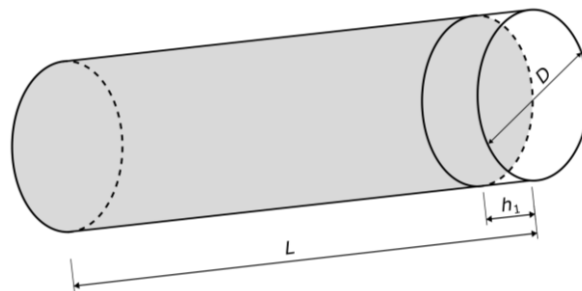


Figure 3: Used geometry of the tested sample.

Figure 3 shows the geometry used with the volume of the empty container with height h_1 on the right-hand side (in experiment this is the top surface of the sample). This volume was left empty to carefully insert the thermocouple's used during the μ CT scanning process. The thermocouple cable was placed in the middle of the lid as close to the centre of the sample as possible to provide accurate temperature data, while allowing sample axial rotation without redundant thermocouple movement. In total, two samples were made to distinguish hydration heat development of cement from external heating from X-ray source.

2.3 Cement Hydration Heat Model

Literature overview provides various analytical models for concrete hydration [11], which could be extended to analysis of heat release influencing the stress of concrete structures structural members [44,45]. In this study a hydration model Schindler [46], which combines RILEM methodology [47] and experimental findings of Hansen [48].

The temperature development produced by concrete specimen during curing period under adiabatic condition can be calculated as:

$$\frac{dT}{dt} = \frac{Q_H}{\rho \cdot c_p} = \frac{dH}{dt} \left(\frac{1}{\rho \cdot c_p} \right) \quad (1)$$

where T is the concrete temperature, ρ is the concrete density, c_p is concrete specific heat capacity, Q_H is the rate of heat generation and H is the heat of hydration of the concrete.

Temperature T from Eq. (1) clearly depends on the heat generation rate Q_H , which could be determined from following expression:

$$Q_H(t) = H_u \cdot C_c \cdot \left(\frac{\tau}{t_e} \right)^\beta \cdot \left(\frac{\beta}{t_e} \right) \cdot \alpha(t_e) \cdot \frac{E}{R} \left(\frac{1}{273 + T_R} - \frac{1}{273 + T_C} \right) \quad (2)$$

where H_u is the total hydration heat of all cementitious materials, C_c is the cementitious materials content, τ is the hydration time parameter, β is the hydration shape parameter, $\alpha(t_e)$ is the degree of hydration at equivalent time t_e , E is activation energy, R is the universal gas constant (8.314 J/mol·K⁻¹) and T_c and T_r is the concrete temperature and reference (room) temperature, respectively. The rate of heat generation Q_H is dependent on degree of hydration $\alpha(t)$, which can be calculated from Eq. (3) as follows:

$$\alpha(t) = \frac{H(t)}{H_T} \quad (3)$$

where $H(t)$ is cumulative heat of hydration released at time t and H_T is the ultimate hydration heat. Ultimate hydration heat H_T can be calculated as $H_T = H_u \cdot C_c$. In this study the Portland cement is used, and based on its chemical composition the hydration heat of cement can be calculated. Thus, the hydration heat of cement H_{CEM} will be used as follows:

$$H_{CEM} = 500p_{C_3S} + 260p_{C_2S} + 866p_{C_3A} + 420p_{C_4AF} + 624p_{SO_3} + 1186p_{FreeCaO} + 850p_{MgO} \quad (4)$$

where H_{CEM} is total heat of hydration of used cement and p_n is weight ratio of n -th compound of the total cement content. The Eq. (4) offers possible adoption to the use of blended cements [46] with content of supplementary cementitious materials (SCMs) e.g., slag, fly ash, metakaolin, etc.

The degree of hydration $\alpha(t_e)$, hydration time and shape parameters τ and β used in Eq. (2) are determined from experimentally from adiabatic or semi-adiabatic calorimetry of hydration heat [47]. The experimental data can be fitted by exponential curve as:

$$\alpha(t_e) = \alpha_u \cdot e^{-\left(\frac{\tau}{t_e} \right)^\beta} \quad (5)$$

where $\alpha(t_e)$ is the degree of hydration at equivalent age time t_e , τ is the hydration time parameter, β is the hydration shape parameter and α_u is the ultimate degree of hydration. The ultimate degree of hydration is unaffected by the concrete curing temperature and sometimes can be calculated based on water to cement ratio w/c .

2.4 X-ray μ CT Test Setup

The radiographical imaging procedure was performed using custom built XCT laboratory system. For this experiment μ XCT is equipped by 20 W Microfocus X-ray source L10321 (Hamamatsu Photonics K.K., Japan), Dexela 1512 NDT (PerkinElmer, Waltham, MA, USA) flat panel X-ray detector with active area of 1944×1536 px (75 μ m pitch) using CMOS technology with Gadolinium oxysulfide scintillator, and rotary table ACD120-80 (Akribis Systems, Singapore) with ± 3 arc sec angular precision. The used test setup for μ CT is shown in Figure 4.

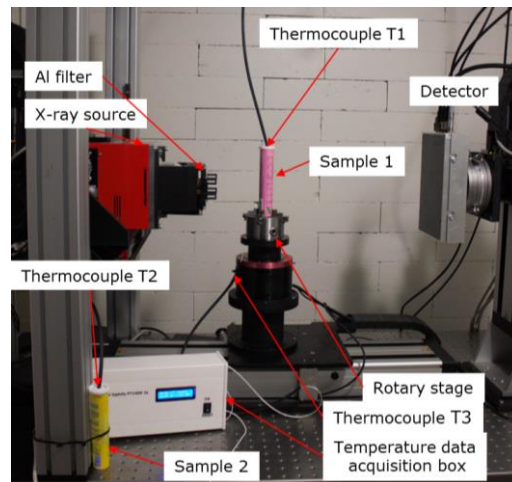


Figure 4: μ XCT test set up with indication to cement mortar samples and used thermocouples.

Figure 4 shows overall view on experimental test setup used for μ XCT data acquisition with marked scanned and reference samples. To acquire comprehensive information of generated heat during the cement hydration, Figure 4 shows high sensitivity thermocouples.

In total, three PT-1000 thermocouples (Kuongshun, China) with a range from $-60^{\circ}\text{C} \sim 200^{\circ}\text{C} \pm 0.05^{\circ}\text{C}$ were used with lengths of 1 m and 5 m, respectively. All thermocouples were connected using a MAX31865 amplifier to the Arduino Due board circuit used in the data acquisition. Such circuit captures temperature data with a frequency of 1 Hz. The positioning of the thermocouples during the experiment was as follows: thermocouple T1) was placed in the scanned sample; thermocouple T2) was placed in the reference sample; and thermocouple T3) was mounted close to the scanned sample, but outside of the X-ray range to measure room temperature.

For the scanning procedure the acceleration voltage of 100 kV and a target current of 175 μ A together with 4 mm Aluminium filter [49] was used to obtain as much as possible high-quality image of the radiograms. Altogether, 20 time-lapse tomographical scans of the consisted of 1436 equiangular projections with 3×175 ms acquisition time. Including positioning and read-out time each tomographical scan takes ~ 17 mins.

The reconstruction of individual 3D images was performed using an Feldkamp–Davis–Kress (FDK) filtered back projection reconstruction algorithm [50] implemented in VG Studio MAX 2023.2.1 (Volume Graphics, Germany) producing 3D data matrices with dimensions of $1943 \times 1943 \times 1536$ voxels (voxel size of 20.6 μ m). This provides region of interest (ROI) with elliptical (circular) cross-section geometry approximately of 26.02×26.16 mm² by 36.14 mm long see Figure 5.

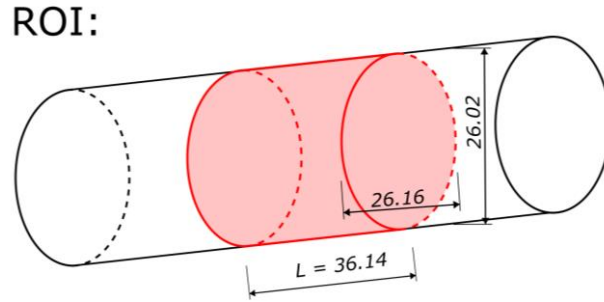


Figure 5: Schematic illustration of the analysed volume by μ CT.

The ROI as presented in Figure 5 was selected to be in the middle of the cylinder outside of the possible reach of the inserted thermocouple. The size of ROI volume is $19\,800\text{ mm}^3$ which will be used in the porosity measurement.

2.5 X-ray μ CT Data

Since the concrete as well as cement mortar are multi-phase heterogeneous materials, a threshold-based segmentation allows to perform phase separation to obtain separated 3D images of either the pore space and the solid phases. The workflow of post-processing μ XCT data is shown in Figure 6.

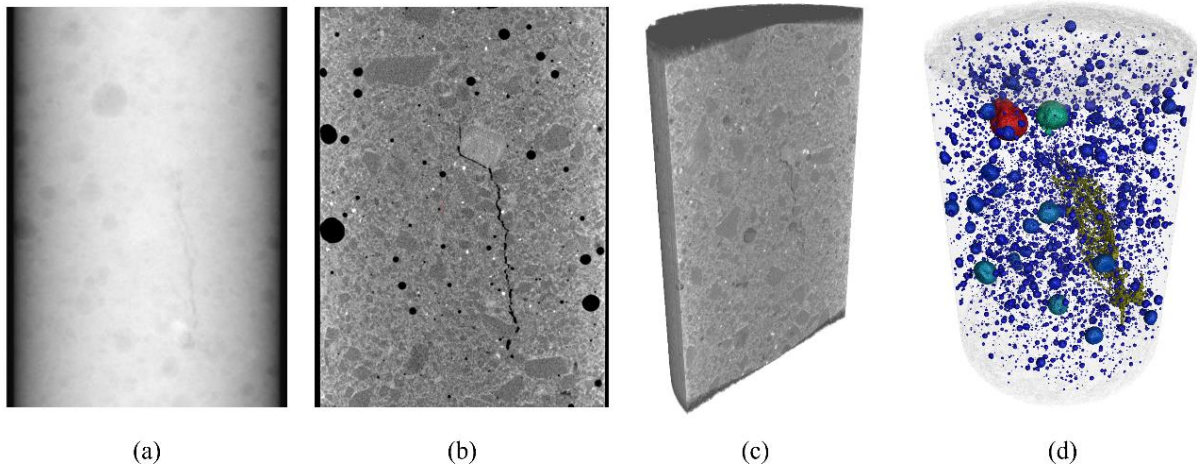


Figure 6: Illustration of obtain X-ray data – (a) raw radiograph, (b) – 2D view of CT reconstructed data, (c) – 3D view on solid phases and (d) – separated pores.

Figure 6 depicts the workflow on the image analysis from the experiment to identification of individual pores. During the experiment and the tomographic scanning of the studied sample, X-ray radiograms showing the specimen X-ray attenuation are acquired (Figure 6(a)). The set of equiangular projections is reconstructed to a 3D image showing specimen density, where Figure 6(b) shows a 2D view on a slice through such reconstructed volume including the pores and the crack. The density information contained in the reconstructed volume enables to study material heterogeneity additionally to the pore space analysis using arbitrary visualisation means as depicted in Figure 6(c). Based on the procedure described in the following section, pore space and the crack can be quantified and visualised to, e.g., to the appearance in Figure 6(d), where the solid phases are suppressed in favour of individual pores and the crack coloured according to their calculated volume.

2.6 Porosity Measurement

To distinguish between pores and rising crack in the studied material, a porosity-space quantification was performed using tools implemented in the reconstruction software. In the first step, the surface of the specimen, i.e., interface between the air and the solid, was identified on the basis of gray-value threshold determined as an Otsu's threshold algorithm [51,52]. After the segmentation, pore

identification procedure based on seed points for individual pore identification with consideration of local gray value variation due to noise in the reconstructed 3D images.

The result of the analysis not only allows to study local variations of porosity and porosity profiles along arbitrary directions in the reconstructed volume of the specimen, but also to extract every individual identified pore as a separate volume additionally to the calculated morphological characteristics. This approach was used to study and visualise the growth of the crack in the initial stages of the experiment. Here, the pore and crack localisation parameters were set on the first CT data post-processing and kept the same throughout the whole experiment, which, coupled with stable long term emission characteristics of the X-ray source and response of the X-ray detector, ensured the highest possible reliability of the porosity quantification.

3. Experimental Results and Discussion

In this section a comprehensive overview of the obtained experimental results is given. We begin with the presentation of measured hydration heat emission obtained from both samples. Afterwards, we present in detail an internal damage analysis using μ XCT scans. The link between changes in the meso-structure during hydration process of OPC was found.

3.1 Hydration Temperature Development

In order to link meso-structural changes due to internal processes related to cement hydration of mixture, temperature of mixture was measured during the experiment over 25 hours. Captured temperature data provide comprehensive information on the hydration process and allowed us to distinguish from the external heat sources. The captured temperature during the μ XCT scanning experiment is shown in Figure 7.

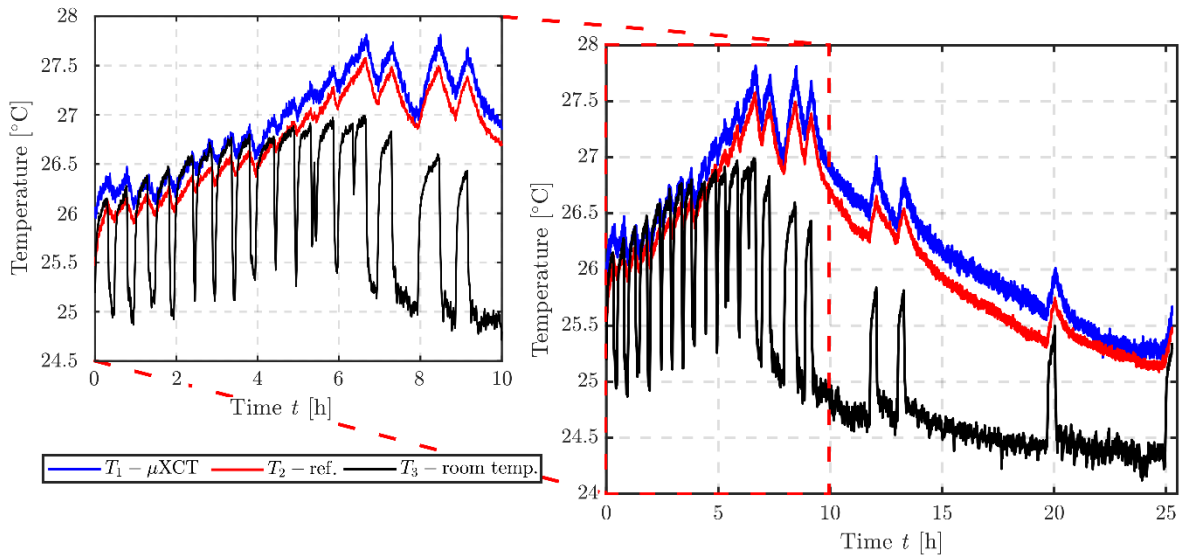


Figure 7: Temperature development over 25 hours of cement hydration with the detail on the first 10 hours.

Figure 7 shows raw temperature data acquired from the T1-T3 thermocouples used during the first 25 hours of cement hydration during the μ XCT scanning experiment. The peaks in the temperature data are related to the start of the μ XCT data acquisition, as the X-ray source produces heat, which results in an increase in the room temperature due to the closure of the X-ray shielding door and its latter opening, respectively. The temperature data for both samples have a similar trend in the first 8 hours. After this period, the measured temperature diverts from each other with a slight increase in the difference between samples keeping this trend until the end of the experiment.

The well-known cement hydration phases are more visible when the room temperature data T_R is subtracted from the measured sample's temperature data T_C of concrete samples as $\Delta T = T_C - T_R$. The

temperature difference ΔT then provides an insight into hydration heat development of both samples and allows us to distinguish an external heat source generated by the X-ray source. The obtained temperature data were smoothed using a moving average filter with a moving window of 2.5 hours as implemented in the MATLAB 2023a (MathWorks, USA) software. The mean temperature difference ΔT data together with original data from both samples are presented in Figure 8.

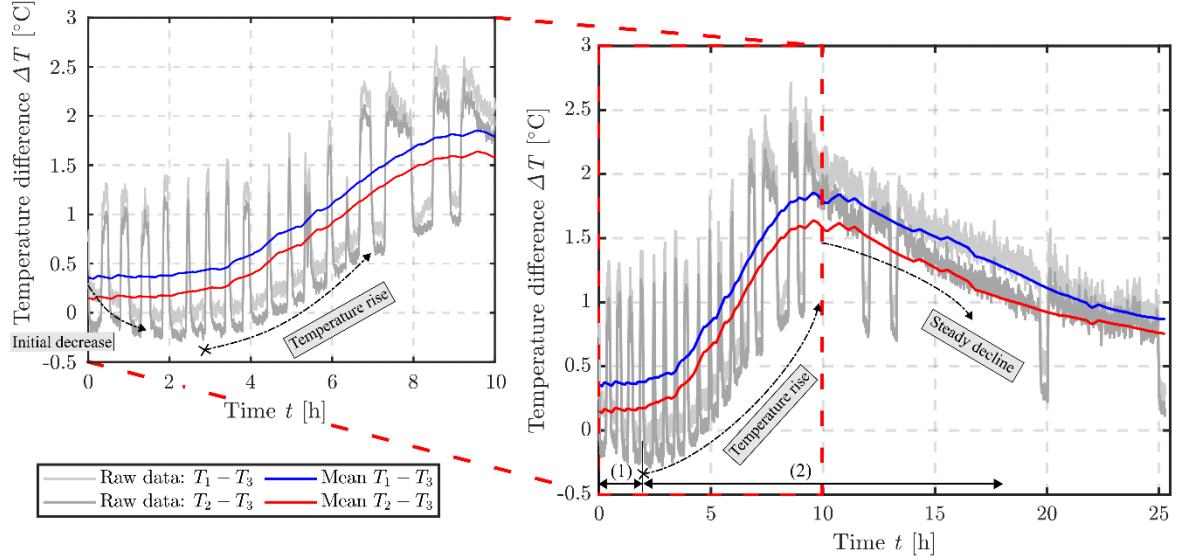


Figure 8: Mean temperature difference ΔT data with the detail on the first 10 hours with indicated hydration phases.

From Figure 8, a clear difference in the measured temperature can be observed between the thermocouple T1 and T2. This difference is approximately 0.3 °C and is again related to the heat produced from the X-ray source since the reference sample was placed outside of the X-ray source range. Please note that the hydration heat as presented in Figure 8 cannot be compared with the adiabatic hydration temperature data shown in Figure 2 as the thermal conditions were different (this includes external heat source from the X-ray and the X-ray shielding door opening).

Careful observation of the raw temperature data as presented in Figure 8, shows a short decrease in hydration heat in the period from 0:00 hours to 0:45 hours after mixing. This is related to the first phase of cement hydration mentioned above. Unfortunately, the initial rapid decrease was not captured due to the sample preparation in another laboratory room (transfer of mixture from mixer to moulds and clamping of the sample in rotary table).

To verify the measured temperature with the analytical prediction as presented in Eq. (1), one needs to acquire chemical composition of the Portland cement used. In this study, we used data available in literature [46], which are similar to used Portland cement CEM I 42.5R type. The adopted chemical composition was measured according to ASTM and is shown in comparison with current cement in Table 4.

Table 4: Chemical composition of ASTM Type I cement adapted from [46].

Type	SiO ₂	Al ₂ O ₃	FeO ₂	CaO	Free CaO	MgO	SO ₃	Na ₂ O + 0.658K ₂ O	C ₃ S	C ₂ S	C ₃ A	C ₄ AF
1	19.9	5.7	2.9	63.6	2.9	1.3	3.5	0.69	57	14	10	8
12	20.9	5	1.8	65.4	1	1.4	2.9	0.52	63	12	10	6
13	20.1	5.3	3.2	65.5	0.8	0.6	3.3	0.67	64	9	8	10
Current	19.0	5.7	2.9	62.6	1.0	-	6.5	1.0 (only K ₂ O)	58	12	9	7

The Table 4 shows similar content of C₃S, C₂S and C₃A of used OPC in current study as presented by Schindler [46] with the difference limited to 6%. Other parameters used in Eq. (2) are presented in Table 5 (please note that these parameters are based on semi-adiabatic process).

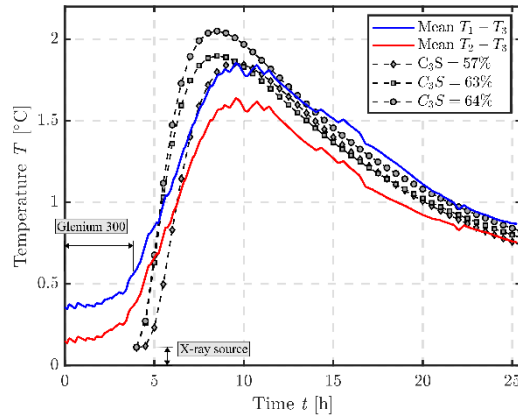
Table 5: Cement hydration model parameters adapted from [46].

No.	Cement type	E [J/mol]	Hydration parameters			H_u [J/g]
			β	τ	α_u	
1	Type I: Source A	45 991	0.905	13.69	0.689	477
12	Type I: Source B	41 977	0.719	16.88	0.887	513
13	Type I: Source C	46 269	0.727	16.32	0.882	492

The study of Schindler [46] provides various fitting parameters, as shown in Table 5, of three cement types based semi-adiabatic calorimetry. In this study, we will use these three cement types as they show similar mineralogical content as the OPC used in this study.

In the analytical prediction of hydration temperature as presented in Eq. (2) concrete temperature T_C was set to 28 °C i.e., measured maximum and room temperature T_R was equal to 23°C. Cement content C_C was $890 \cdot 10^3 \text{ g/m}^3$, which is equivalent to amount used in studied mortar. The concrete density ρ and heat conductivity c_p was $2400 \text{ kg}\cdot\text{m}^3$ and $837 \text{ J/kg}\cdot\text{K}^{-1}$, respectively.

The target power of the X-ray source of approx. 17.5 W was added to the total specimen volume. Thus, the total heat considered in analytical prediction corresponds to $Q_{\text{tot}} = Q_H + Q_{\text{X-ray}}$ and it was used in Eq. (1) to predict hydration temperature of the sample. The comparison of measured and calculated temperature of samples is presented in Figure 9.

**Figure 9:** Comparison of measured and analytically predicted cement hydration temperature of studied sample.

An interesting observation in Figure 9 can be made between experimental and analytical hydration temperature, as the analytical prediction is capable to capture experimentally measured temperature with relatively good agreement. Additionally, Figure 9 shows dependency of hydration heat on the C_3S content. The predicted temperature for 57% of C_3S is capable to predict the temperature peak during the hydration heat most accurately, while other curves for 63% and 64% of C_3S show only similar trend with reasonable error in peak temperature. Moreover, the predicted temperature is capable to include the above discussed external heating of the X-ray source and in this case, it is approximately of 0.3 °C. The delay in time in hydration temperature rise in phase (2) is related to the use of plasticizer Glenium 300, which delays the onset of hydration in second phase by approx. 3.5 hours as observed in adiabatic calorimetry.

This good agreement between analytical and experimental hydration temperature development as presented in Figure 9, serves as a clear link to the meso-structural analysis and further damage localisation and verifies behaviour of used OPC.

3.2 Porosity measurement

Using the implemented algorithms that use gray intensity contrast-based algorithms and knowing the size of ROI, a porosity of the sample can be calculated. The combination of instrumentation used in the experiments and the software tools is able to detect pores with size bigger than the spatial resolution of $20.5 \mu\text{m}/\text{Voxel}$. The pores with size smaller than the spatial resolution are considered as a noise. Typical

results of porosity analysis are the total pore volume, from which the porosity is calculated. In this study, the porosity measurement was done for every acquired μ XCT scan, i.e., 20 porosity calculations. The calculated sample's porosity over the time is presented in Figure 10.

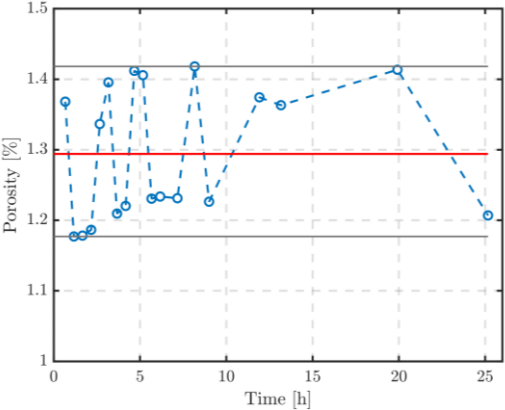


Figure 10: Obtained porosity measurement during the μ CT.

Figure 10 shows obtained porosity of scanned sample throughout the experiment. At first, the result of calculated porosity shows high scatter with changing values nearly every CT scan. However, after performing simple statistics, the mean porosity is $1.29\% \pm 0.12\%$, which is in compliance with the results presented in Figure 10.

The identified pores appear in the samples during pouring mixture to the mould, which agrees with the general expectation as the pores do not arise due to inner chemical reaction during cement hydration. The obtain values of porosity correspond to values found in literature [53,54] ranging from 1% to 4% depending on thy type of concrete.

The scatter in porosity at early age (up to 10 hours) is related to studied hydration process as the wet cement mortar is drying, which results in in changes in threshold values difference. Nonetheless, the porosity measurement in all studied is within reasonable range and provides useful information on the hydration process of cement mortar. Please note that in the calculation of porosity, only pores were included i.e., without localised crack (see next subsection).

3.3 μ XCT – Damage Analysis

Using same approach as for porosity measurement, the damage i.e., cracks, present in the sample could be identified throughout the experiment. In this case, a major crack was detected at 00:40 hours from mixing the samples, which increased in the size to experiment time of 06:10h. After that, the change in crack size was insignificant for the analysis. The μ XCT damage analysis provides valuable information on the crack surface and crack volume development during hydration. The obtained crack surface is presented in Figure 11(a), while the crack volume is shown in Figure 11(b).

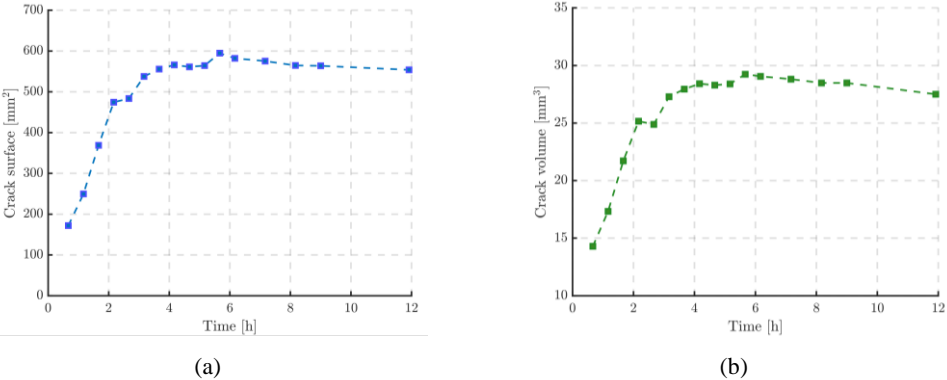


Figure 11: Crack surface development (a) and (b) crack volume development during the CT experiment.

Crack surface and crack volume development as presented in Figure 11 show rapid increase in its size during first 4 hours of the experiment. We link this rapid damage progress in the sample to the onset of second hydration phase (after dormant period) as presented in Figure 8. Although, the temperature data shows steady increase until the age of approx. 10 hours, the crack growth do not progress further after the age of 6 hours. Thus, this time was set as a final crack length, which do not grow any further.

This observed crack growth is more visible, when presented as a 3D data in the obtained ROI. In such visualisation, one can observe pores and solid phases of cement mortar together with the detected crack. 3D Visualisation of detected crack is shown in Figure 12.

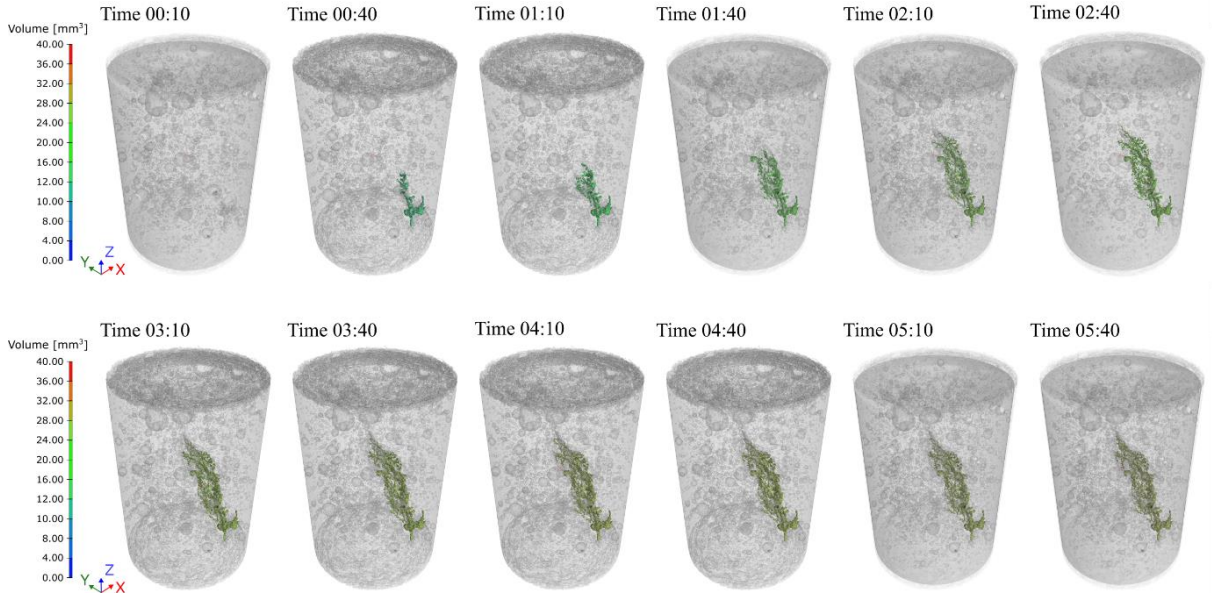


Figure 12: 3D visualisation of detected crack at various age.

Figure 12 shows in-situ crack growth throughout the experiment from 00:10 to 5:40 hours. The first CT (top left) scan shows volume with pores without any cracks. The onset of crack growth appears at time 0:40 hours from the mixing of the sample, which can be again related to the second phase of cement hydration i.e., steady increase in the internal temperature. Another visualisation clearly presents crack growth located inside of the sample, close to specimen centre, without any connection to specimens’ walls.

An interesting observation can be made from Figure 12 in which the crack grows diagonally towards the top side of the specimen. After 5:40 hours of sample’s age, the crack growth stops , or the detected growth is insignificant. Every detected crack in single μ XCT data can be located in the ROI space. The final crack size at 06:10 h age is shown in Figure 13(a), while the schematic illustration of the crack with centre of gravity C_g is shown in Figure 13(b).

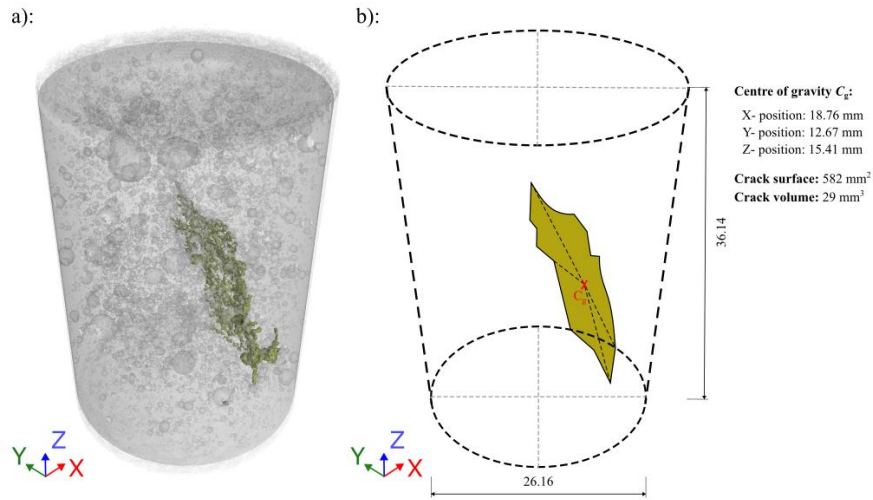


Figure 13: Final crack size at 06:10 hours visualized as 3D CT data (a) and (b) as schematic illustration.

The final crack size at 6:00 hours, as presented in 12(a), shows an interconnection of multiple pores with crack growth in the diagonal direction towards the top edge of the sample. On the other hand, this complex shape could be simplified for better interpretation as a single sketch as shown in Figure 13(b), from which a clear location in the ROI can be made. The measured maximum crack surface and volume was 582 mm² and 29 mm³, respectively. Measured porosity, crack surface and volume are presented in more detail in Appendix A – Experimental Details.

Additionally, the damage analysis detects the crack throughout the experiment, and it provides the information about the coordinates in Cartesian coordinate system of selected ROI. The identified coordinates of the crack's centre of gravity C_g are complemented with the crack surface and crack volume.

Identification of the crack coordinates on every μ XCT scan obtained in this study, allows direct location of the crack's centre of gravity C_g . The obtained coordinates of the centre of gravity C_g throughout the experiment, i.e. at different time, can be interpreted as a crack movement in time. The overall position of the C_g centre of gravity during the μ XCT experiment is presented in Figure 14.

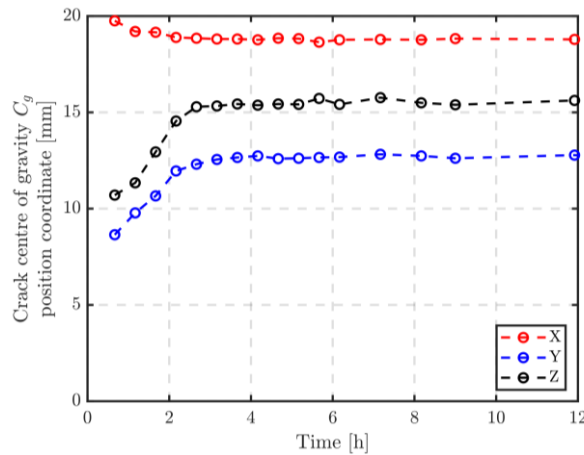


Figure 14: Position of centre of gravity C_g of identified crack.

The results of the crack movement from Figure 14 confirm the observation made from the 3D crack visualisation (Figure 12). The crack grows in the Y-Z plane in the diagonal direction with a similar gradient of both coordinates. The information about the crack's centre of gravity C_g could be used to characterise crack growth from the start of the μ XCT scanning or to describe crack growth between each

μ XCT scan. This information of the increase in crack size from the onset of the fracture is shown in Figure 15(a), while Figure 15(b) shows the increment in crack size between single μ XCT scans.

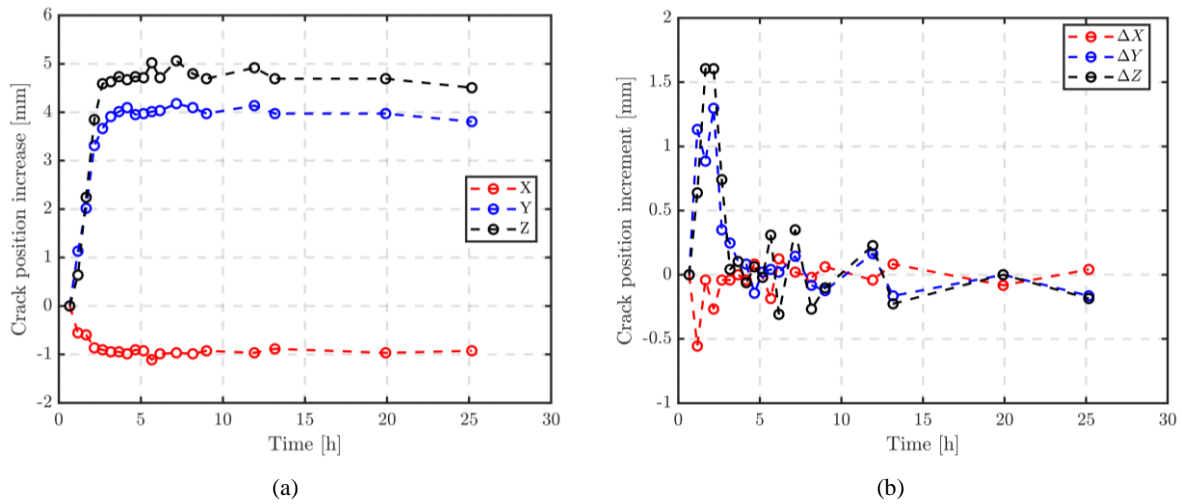


Figure 15: Crack coordinates increase from initial size (a) and (b) crack increment between each CT scan.

The results of the crack's centre of gravity C_g coordinates in Figure 15 confirm previous observations and give a more accurate confirmation of diagonal crack growth, as the increment of the crack is nearly similar for both Y and Z -coordinates. The crack location increment in Figure 15(b) again confirms the observation of crack growth made with connection to the temperature data, which shows the increase in crack size in the period from 0:40 to 2:40 hours, which is considered as a second phase of cement hydration. The negative value of the X -coordinate is related to the interconnection of crack with pores, which gives a more spatial crack shape than common planner crack shape.

Using in situ μ XCT scanning with combination of temperature data provides a valuable insight to the inner cracking process initiated by the natural process of exothermic cement hydration.

Conclusions

This experimental study revisited the hydration of Portland cement, this time focusing on the internal changes in the material. For this, samples of cement mortar were made and place in the X-Ray μ CT imaging setup. μ XCT images were taken during the mortar hardening and hydration heat was measured over 25 hours of cement hydration. Prior to μ XCT scanning, the adiabatic hydration heat was measured of studied mortars, and the chemical and mineralogical analysis of used OPC was determined. With this, we were able to create a timelapse of the damage evolution in the inner structure of the material.

The measured hydration heat was compared with analytical prediction, which was calculated based on the chemical composition of used Portland cement. A relatively good agreement was obtained between the experimental and analytical predictions. This verified the standard behaviour of cement hydration and the consequent cement hardening. Additionally, an X-ray heat source was added to the development of the hydration heat, which increased the accuracy between the analytical and experimental values.

Post-processing of μ XCT data allowed to separate material phases, measure sample's porosity, and most importantly, separate pores from crack. Therefore, porosity was measured at various age from the mortar mixing and the obtained value of 1.29 % corresponds to the standard value of porosity concrete. The observed scatter in the porosity measurement is due to the drying of wet cement mortar, which influenced the values of grayscale threshold used in the pores detection.

Moreover, post-processing of μ XCT data localised crack that was increasing in size from 0:40 to 6:10 hours, after that the crack size change was insignificant. The crack analysis was provided with the location of the centre of gravity C_g , which was changing in time during the μ XCT experiment. Hence,

the change in the centre of gravity C_g of the crack could be interpreted as a crack growth. Furthermore, the crack surface and crack volume were calculated throughout the μ XCT experiment. The observed internal crack growth was related to the hydration temperature, which allowed a comprehensive understanding of the studied process.

Found experimental results can contribute to understanding of the damage initiation caused by the natural process of Portland cement hydration as well as to the understanding the shrinkage behaviour of the mortar.

Acknowledgements

Financial support provided by the Czech Science Foundation under project no. 21-08772S provided material, as well as under the project no. 23-05128S, which provided the μ XCT equipment and consequent μ XCT data post-processing.

This paper was created as part of the project No. CZ.02.01.01/00/22_008/0004631 Materials and technologies for sustainable development within the OP JAK Program financed by the European Union and from the state budget of the Czech Republic.

CRediT authorship contribution statement

Petr Miarka: Visualization, Investigation, Funding acquisition, Conceptualization, Writing – original draft. **Daniel Kytýř:** Visualization, Data curation, Writing – review & editing, Funding acquisition. **Petr Koudelka:** Methodology, Visualization, Data curation, Writing – review & editing, Validation, Funding acquisition, Formal analysis. **Vlastimil Bílek:** Supervision, Formal analysis, Funding acquisition, Writing – review & editing.

Data availability

The data used in this study is available at: [10.5281/zenodo.10390883](https://doi.org/10.5281/zenodo.10390883)

Supplementary material available at: <https://imgur.com/sDWozsW>
<https://i.imgur.com/sDWozsW.mp4>

Appendix A – Experimental Details

The measured dimensions and calculated total volume of studied specimens are shown in Table A1 - 1.

Table A1 - 1: Measured dimension and calculated total volume.

	Diameter D [mm]	Length L [mm]	h_1 [mm]	Volume [mm ³]
Reference sample	28.9	144.74	25.6	78 152.55
Test sample	28.9	142.8	19.0	81 209.38

To give comprehensive overview of measured porosity and detected crack surfaces and volumes throughout the experiment is shown in Table A1 - 2.

Table A1 - 2: Measured pore volume corresponding porosity, crack surface and crack surface obtained by μ CT.

Duration [h]	Pore volume [mm ³]	Porosity [%]	Crack volume [mm ³]	Crack surface [mm ²]
0:30	264.34	1.37	14.29	171.86
1:00	227.41	1.18	17.33	249.53
1:30	227.64	1.18	21.71	368.79
2:00	229.23	1.19	25.16	474.53
2:30	258.22	1.34	24.88	483.49
3:00	269.62	1.40	27.29	537.64
3:30	233.68	1.21	27.95	555.75
4:00	235.78	1.22	28.41	565.93
4:30	272.79	1.41	28.29	561.10
5:00	271.59	1.41	28.40	564.32
5:30	237.77	1.23	29.24	594.80
6:00	238.36	1.23	29.05	582.10
6:30	237.89	1.23	28.81	575.31
7:00	273.99	1.42	28.48	564.62
8:00	236.94	1.23	28.48	563.73
9:00	265.52	1.37	27.50	553.84
12:00	263.37	1.36	27.02	540.77
20:00	273.09	1.41	28.48	567.13
25:00	233.17	1.21	25.12	513.62

References

- [1] E.G. Nawy, *Fundamentals of High-Performance Concrete*, Wiley, 2001. <https://books.google.be/books?id=W6BNygdZLJUC>.
- [2] M.A. Caldarone, *High-Strength Concrete: A Practical Guide*, CRC Press, 2019. <https://www.crcpress.com/High-Strength-Concrete-A-Practical-Guide/Caldarone/p/book/9780367386917#googlePreviewContainer>.
- [3] S.A. Miller, V.M. John, S.A. Pacca, A. Horvath, Carbon dioxide reduction potential in the global cement industry by 2050, *Cem Concr Res.* 114 (2018) 115–124. <https://doi.org/10.1016/J.CEMCONRES.2017.08.026>.
- [4] G. Habert, S.A. Miller, V.M. John, J.L. Provis, A. Favier, A. Horvath, K.L. Scrivener, Environmental impacts and decarbonization strategies in the cement and concrete industries, *Nature Reviews Earth & Environment* 2020 1:11. 1 (2020) 559–573. <https://doi.org/10.1038/s43017-020-0093-3>.
- [5] M. Schneider, The cement industry on the way to a low-carbon future, *Cem Concr Res.* 124 (2019) 105792. <https://doi.org/10.1016/J.CEMCONRES.2019.105792>.
- [6] M. Nedeljković, J. Visser, B. Šavija, S. Valcke, E. Schlangen, Use of fine recycled concrete aggregates in concrete: A critical review, *Journal of Building Engineering.* 38 (2021) 102196. <https://doi.org/10.1016/J.JOBE.2021.102196>.
- [7] W. Chen, R. Jin, Y. Xu, D. Wanatowski, B. Li, L. Yan, Z. Pan, Y. Yang, Adopting recycled aggregates as sustainable construction materials: A review of the scientific literature, *Constr Build Mater.* 218 (2019) 483–496. <https://doi.org/10.1016/J.CONBUILDMAT.2019.05.130>.
- [8] P.-C. Aïtcin, R.J. Flatt, *Science and technology of concrete admixtures*, Woodhead publishing, 2015.
- [9] J. Bensted, Hydration of Portland Cement, *Advances in Cement Technology.* (1983) 307–347. <https://doi.org/10.1016/B978-0-08-028670-9.50015-6>.
- [10] D. Jansen, F. Goetz-Neunhoeffler, B. Lothenbach, J. Neubauer, The early hydration of Ordinary Portland Cement (OPC): An approach comparing measured heat flow with calculated heat flow from QXRD, *Cem Concr Res.* 42 (2012) 134–138. <https://doi.org/10.1016/J.CEMCONRES.2011.09.001>.
- [11] K. Van Breugel, Simulation of hydration and formation of structure in hardening cement-based materials, (1997). <https://repository.tudelft.nl/islandora/object/uuid%3A68a3331c-5c83-4009-ac29-aa87cbc4afb8> (accessed November 8, 2023).
- [12] R. François, S. Laurens, F. Deby, *Corrosion and its Consequences for Reinforced Concrete Structures*, Elsevier, 2018. <https://doi.org/10.1016/B978-1-78548-234-2.50009-3>.
- [13] N. Roussel, *Understanding the Rheology of Concrete*, Woodhead Publishing, Buckingham, England, UK, 2012. <https://www.sciencedirect.com/book/9780857090287/understanding-the-rheology-of-concrete>.
- [14] S. Ghourchian, M. Wyrzykowski, M. Plamondon, P. Lura, On the mechanism of plastic shrinkage cracking in fresh cementitious materials, *Cem Concr Res.* 115 (2019) 251–263. <https://doi.org/10.1016/J.CEMCONRES.2018.10.015>.
- [15] D.S. Kurup, M.K. Mohan, K. Van Tittelboom, G. De Schutter, M. Santhanam, A. V. Rahul, Early-age shrinkage assessment of cementitious materials: A critical review, *Cem Concr Compos.* 145 (2024) 105343. <https://doi.org/10.1016/J.CEMCONCOMP.2023.105343>.

- [16] Z. Hashin, P.J.M. Monteiro, An inverse method to determine the elastic properties of the interphase between the aggregate and the cement paste, *Cem Concr Res.* 32 (2002) 1291–1300. [https://doi.org/10.1016/S0008-8846\(02\)00792-5](https://doi.org/10.1016/S0008-8846(02)00792-5).
- [17] L. Cedolin, S.D. Poli, I. Iori, Tensile Behavior of Concrete, *J Eng Mech.* 113 (1987) 431–449. [https://doi.org/10.1061/\(ASCE\)0733-9399\(1987\)113:3\(431\)](https://doi.org/10.1061/(ASCE)0733-9399(1987)113:3(431)).
- [18] L. Cedolin, S. Dei Poli, I. Iori, Experimental determination of the fracture process zone in concrete, *Cem Concr Res.* 13 (1983) 557–567. [https://doi.org/10.1016/0008-8846\(83\)90015-7](https://doi.org/10.1016/0008-8846(83)90015-7).
- [19] S. Muralidhara, B.K.R. Prasad, H. Eskandari, B.L. Karihaloo, Fracture process zone size and true fracture energy of concrete using acoustic emission, *Constr Build Mater.* 24 (2010) 479–486. <https://doi.org/10.1016/j.conbuildmat.2009.10.014>.
- [20] S. Bhowmik, S. Ray, An experimental approach for characterization of fracture process zone in concrete, *Eng Fract Mech.* 211 (2019) 401–419. <https://doi.org/10.1016/J.ENGFRACTMECH.2019.02.026>.
- [21] P. Miarka, A.S. Cruces, P. Lopez-Crespo, W. De Corte, Fracture process zone development and length assessment under the mixed-mode I/II load analysed by digital image correlation technique, *Cem Concr Res.* 173 (2023) 107261. <https://doi.org/10.1016/J.CEMCONRES.2023.107261>.
- [22] S. Das, M. Aguayo, G. Sant, B. Mobasher, N. Neithalath, Fracture process zone and tensile behavior of blended binders containing limestone powder, *Cem Concr Res.* 73 (2015) 51–62. <https://doi.org/10.1016/j.cemconres.2015.03.002>.
- [23] H.T. Kim, D.F.T. Razakamandimby R., V. Szilágyi, Z. Kis, L. Szentmiklósi, M.A. Glinicki, K. Park, Reconstruction of concrete microstructure using complementarity of X-ray and neutron tomography, *Cem Concr Res.* 148 (2021) 106540. <https://doi.org/10.1016/J.CEMCONRES.2021.106540>.
- [24] D. Snoeck, W. Goethals, J. Hovind, P. Trtik, T. Van Mullem, P. Van den Heede, N. De Belie, Internal curing of cement pastes by means of superabsorbent polymers visualized by neutron tomography, *Cem Concr Res.* 147 (2021) 106528. <https://doi.org/10.1016/J.CEMCONRES.2021.106528>.
- [25] K. Otsuka, H. Date, Fracture process zone in concrete tension specimen, *Eng Fract Mech.* 65 (2000) 111–131. [https://doi.org/10.1016/S0013-7944\(99\)00111-3](https://doi.org/10.1016/S0013-7944(99)00111-3).
- [26] I. Kumpova, M. Vopalensky, T. Fila, D. Kytir, D. Vavrik, M. Pichotka, J. Jakubek, Z. Kersner, J. Klon, S. Seidl, J. Sobek, On-the-Fly Fast X-Ray Tomography Using a CdTe Pixelated Detector - Application in Mechanical Testing, *IEEE Trans Nucl Sci.* 65 (2018) 2870–2876. <https://doi.org/10.1109/TNS.2018.2873830>.
- [27] S.Y. Chung, J.S. Kim, D. Stephan, T.S. Han, Overview of the use of micro-computed tomography (micro-CT) to investigate the relation between the material characteristics and properties of cement-based materials, *Constr Build Mater.* 229 (2019) 116843. <https://doi.org/10.1016/J.CONBUILDMAT.2019.116843>.
- [28] C.M. Loeffler, Y. Qiu, B. Martin, W. Heard, B. Williams, X. Nie, Detection and segmentation of mechanical damage in concrete with X-Ray microtomography, *Mater Charact.* 142 (2018) 515–522. <https://doi.org/10.1016/J.MATCHAR.2018.06.018>.
- [29] S.Y. Chung, M. Abd Elrahman, J.S. Kim, T.S. Han, D. Stephan, P. Sikora, Comparison of lightweight aggregate and foamed concrete with the same density level using image-based characterizations, *Constr Build Mater.* 211 (2019) 988–999. <https://doi.org/10.1016/J.CONBUILDMAT.2019.03.270>.

- [30] Skarżyński, M. Nitka, J. Tejchman, Modelling of concrete fracture at aggregate level using FEM and DEM based on X-ray μ CT images of internal structure, *Eng Fract Mech.* 147 (2015) 13–35. <https://doi.org/10.1016/J.ENGFRACTMECH.2015.08.010>.
- [31] W. Trawiński, J. Bobiński, J. Tejchman, Two-dimensional simulations of concrete fracture at aggregate level with cohesive elements based on X-ray μ CT images, *Eng Fract Mech.* 168 (2016) 204–226. <https://doi.org/10.1016/J.ENGFRACTMECH.2016.09.012>.
- [32] J. Huang, K. Krabbenhoft, A. V. Lyamin, Statistical homogenization of elastic properties of cement paste based on X-ray microtomography images, *Int J Solids Struct.* 50 (2013) 699–709. <https://doi.org/10.1016/J.IJSOLSTR.2012.10.030>.
- [33] S.Y. Chung, P. Sikora, D.J. Kim, M.E. El Madawy, M. Abd Elrahman, Effect of different expanded aggregates on durability-related characteristics of lightweight aggregate concrete, *Mater Charact.* 173 (2021) 110907. <https://doi.org/10.1016/J.MATCHAR.2021.110907>.
- [34] T.J. Chotard, A. Smith, M.P. Boncoeur, D. Fargeot, C. Gault, Characterisation of early stage calcium aluminate cement hydration by combination of non-destructive techniques: acoustic emission and X-ray tomography, *J Eur Ceram Soc.* 23 (2003) 2211–2223. [https://doi.org/10.1016/S0955-2219\(03\)00082-7](https://doi.org/10.1016/S0955-2219(03)00082-7).
- [35] T.J. Chotard, M.P. Boncoeur-Martel, A. Smith, J.P. Dupuy, C. Gault, Application of X-ray computed tomography to characterise the early hydration of calcium aluminate cement, *Cem Concr Compos.* 25 (2003) 145–152. [https://doi.org/10.1016/S0958-9465\(01\)00063-4](https://doi.org/10.1016/S0958-9465(01)00063-4).
- [36] X. Li, Q. Hu, B. Robertson, M. Tyler Ley, X. Xiao, Direct observation of C3S particles greater than 10 μ m during early hydration, *Constr Build Mater.* 369 (2023) 130548. <https://doi.org/10.1016/J.CONBUILDMAT.2023.130548>.
- [37] D. Gastaldi, F. Canonico, L. Capelli, E. Boccaleri, M. Milanesio, L. Palin, G. Croce, F. Marone, K. Mader, M. Stampanoni, In situ tomographic investigation on the early hydration behaviors of cementing systems, *Constr Build Mater.* 29 (2012) 284–290. <https://doi.org/10.1016/J.CONBUILDMAT.2011.10.016>.
- [38] I. Kumpova, T. Fila, D. Vavrik, Z. Kersner, X-ray dynamic observation of the evolution of the fracture process zone in a quasi-brittle specimen, *Journal of Instrumentation.* 10 (2015) C08004. <https://doi.org/10.1088/1748-0221/10/08/C08004>.
- [39] D. Vavrik, P. Benes, T. Fila, P. Koudelka, I. Kumpova, D. Kytir, M. Vopalensky, M. Vavro, L. Vavro, Local fracture toughness testing of sandstone based on X-ray tomographic reconstruction, *International Journal of Rock Mechanics and Mining Sciences.* 138 (2021) 104578. <https://doi.org/10.1016/J.IJRMMS.2020.104578>.
- [40] S.H. Shim, T.H. Lee, S.J. Yang, N.B.M. Noor, J.H.J. Kim, Calculation of Cement Composition Using a New Model Compared to the Bogue Model, *Materials* 2021, Vol. 14, Page 4663. 14 (2021) 4663. <https://doi.org/10.3390/MA14164663>.
- [41] R.H. Bogue, Calculation of the Compounds in Portland Cement, *Industrial and Engineering Chemistry - Analytical Edition.* 1 (1929) 192–197. https://doi.org/10.1021/AC50068A006/ASSET/AC50068A006.FP.PNG_V03.
- [42] A.M. Neville, Properties of concrete, (2011). https://books.google.com/books/about/Properties_of_Concrete.html?hl=cs&id=mmygngEACA-AJ (accessed November 10, 2023).
- [43] P.C. Aïtcin, High-Performance Concrete, *High-Performance Concrete.* (2011) 1–591. <https://doi.org/10.4324/9780203475034/HIGH-PERFORMANCE-CONCRETE-PIERRE-CLAUDE-A>.

- [44] T.A. Do, H.L. Chen, G. Leon, T.H. Nguyen, A combined finite difference and finite element model for temperature and stress predictions of cast-in-place cap beam on precast columns, *Constr Build Mater.* 217 (2019) 172–184. <https://doi.org/10.1016/J.CONBUILDMAT.2019.05.019>.
- [45] T.A. Do, T.T. Hoang, T. Bui-Tien, H.V. Hoang, T.D. Do, P.A. Nguyen, Evaluation of heat of hydration, temperature evolution and thermal cracking risk in high-strength concrete at early ages, *Case Studies in Thermal Engineering.* 21 (2020) 100658. <https://doi.org/10.1016/J.CSITE.2020.100658>.
- [46] A.K. Schindler, K.J. Folliard, Heat of Hydration Models for Cementitious Materials, *Materials Journal.* 102 (2005) 24–33. <https://doi.org/10.14359/14246>.
- [47] RILEM 119-TCE, Adiabatic and Semi-Adiabatic Calorimetry to Determine the Temperature Increase in Concrete due to Hydration Heat of Cement, *RILEM Report 15.* (1999) 315–330.
- [48] I. Pane, W. Hansen, Concrete Hydration and Mechanical Properties under Nonisothermal Conditions, *Materials Journal.* 99 (2002) 534–542. <https://doi.org/10.14359/12362>.
- [49] G.E. Campillo-Rivera, C.O. Torres-Cortes, J. Vazquez-Bañuelos, M.G. Garcia-Reyna, C.A. Marquez-Mata, M. Vasquez-Arteaga, H.R. Vega-Carrillo, X-ray spectra and gamma factors from 70 to 120 kV X-ray tube voltages, *Radiation Physics and Chemistry.* 184 (2021) 109437. <https://doi.org/10.1016/J.RADPHYSHEM.2021.109437>.
- [50] H. Miao, H.J. Zhao, F. Gao, S.R. Gong, Implementation of FDK reconstruction algorithm in cone-beam CT based on the 3D Shepp-Logan Model, *Proceedings of the 2009 2nd International Conference on Biomedical Engineering and Informatics, BMEI 2009.* (2009). <https://doi.org/10.1109/BMEI.2009.5304987>.
- [51] N. Otsu, THRESHOLD SELECTION METHOD FROM GRAY-LEVEL HISTOGRAMS., *IEEE Trans Syst Man Cybern. SMC-9* (1979) 62–66. <https://doi.org/10.1109/TSMC.1979.4310076>.
- [52] D.Y. Huang, C.H. Wang, Optimal multi-level thresholding using a two-stage Otsu optimization approach, *Pattern Recognit Lett.* 30 (2009) 275–284. <https://doi.org/10.1016/J.PATREC.2008.10.003>.
- [53] Z. Yu, G. Ye, The pore structure of cement paste blended with fly ash, *Constr Build Mater.* 45 (2013) 30–35. <https://doi.org/10.1016/J.CONBUILDMAT.2013.04.012>.
- [54] R. Kumar, B. Bhattacharjee, Porosity, pore size distribution and in situ strength of concrete, *Cem Concr Res.* 33 (2003) 155–164. [https://doi.org/10.1016/S0008-8846\(02\)00942-0](https://doi.org/10.1016/S0008-8846(02)00942-0).